CHAOS **28**, 045109 (2018)

Collective orientational dynamics of pinned chemically-propelled nanorotors

Bryan Robertson,[1,a)] Holger Stark,[2,b)] and Raymond Kapral[1,2,c)]
[1]*Chemical Physics Theory Group, Department of Chemistry, University of Toronto, Toronto, Ontario M5S 3H6, Canada*
[2]*Institut für Theoretische Physik, Technische Universität Berlin, Hardenbergstrasse 36, 10623 Berlin, Germany*

(Received 5 December 2017; accepted 1 February 2018; published online 6 April 2018)

Collections of chemically propelled nanomotors free to move in solution can form dynamic clusters with diverse properties as a result of interactions through hydrodynamic flow and concentration fields, as well as direct intermolecular interactions between motors. Here, we study the collective rotational behavior of pinned sphere-dimer motors where direct motor-motor interactions play no role. Since the centers of mass of the motors are pinned, they cannot execute directed translational motion, but they can pump fluid and rotate; thus, the rotors remain coupled through hydrodynamic and chemical fields. Using a microscopic simulation method that accounts for coupling through both these fields, we show that different rotor configurations with a high degree of correlation exist and their forms depend on the nature of the fluid-rotor interactions. The correlations are greatly reduced or completely destroyed when the chemical interactions are removed, indicating that hydrodynamic coupling, while present, plays a lesser role in determining the collective rotor dynamics. These conclusions are supported by Langevin dynamics simulations that neglect hydrodynamics and include an approximate form of coupling through chemical fields. *Published by AIP Publishing.* https://doi.org/10.1063/1.5018297

Active matter, where some of the constituent species are self-propelled or externally forced, has properties that differ from those of systems at equilibrium. These nonequilibrium systems are the rule rather than the exception in nature, and biology provides many examples where molecular machines or microorganisms move autonomously. Active matter made from synthetic motors is under active study since it may be used for applications on small scales that are not possible for equilibrium systems. This work focuses on one aspect of such active systems: how collective orientational dynamics occurs when synthetic chemically powered motors are pinned to a substrate.

I. INTRODUCTION

Molecular machines and nanoscale motors operate in nonequilibrium environments by converting energy sources in their surroundings into useful work, often in the form of directed motion.[1] The physics underlying the dynamics of such objects is fundamentally different from that of their macroscopic counterparts; for example, these motors and machines move in low Reynolds number environments where viscous drag dominates inertia[2] and random thermal fluctuations must be taken into account. Many mechanisms govern the operation of naturally occurring and synthetic motors, giving rise to a large variety of active systems with rich and complex dynamics.

This variety is most easily observed in Nature itself, such as the motion of kinesin walking along microtubules driven by adenosine triphosphate hydrolysis or microorganism swimming by asymmetrical flagellar motions.[3] Such a variety also exists within the realm of synthetic motors, including motors that move through asymmetric, cyclic, conformational changes and rigid motors propelled by the expulsion of bubbles or phoretic mechanisms.[4–7] Systems of such motors are examples for active matter, which have been shown to display diverse types of collective behavior, different from that in equilibrium systems.[8–12]

Chemically self-propelled nanorod motors that operate by self-electrophoresis were first synthesized over a decade ago. Initial experiments observed motors that move in solution in a directed fashion and motors attached to a surface that acted as fixed rotors.[13,14] Current research centers on understanding general aspects of directed motor motion through experiment and theory.[4] There have been several experimental investigations of the collective dynamics of chemically propelled motors.[15–19] Theoretical models including interactions through chemical gradients but neglecting hydrodynamic interactions have been constructed and studied.[20–24] Microscopic simulations,[25–27] as well as a lattice-Boltzmann simulation,[28] that include both the chemical gradient and hydrodynamic coupling effects have also been carried out. Such studies have shown that these systems may undergo active self-assembly to form diverse types of dynamic clusters and other structures and segregate into domains of high and low density motor states with distinctive properties.

Our focus in this article is on the collective dynamics of pinned synthetic chemically powered motors that operate by

---

[a)]Electronic mail: bryan.robertson@mail.utoronto.ca
[b)]Electronic mail: holger.stark@tu-berlin.de
[c)]Electronic mail: rkapral@chem.utoronto.ca

a self-diffusiophoretic mechanism. Section II describes the diffusiophoretic mechanism for the dynamics of pinned and unpinned sphere-dimer motors. The results of simulations of the collective dynamics of pinned motors using a coarse-grain microscopic dynamical method that combines molecular dynamics of motors with multiparticle collision dynamics of the fluid are presented in Sec. III. Section IV compares the results of the microscopic simulations with those of a Langevin model for the dynamics that incorporates interactions through chemical gradients but neglects hydrodynamic interactions. The conclusions of this paper are given in Sec. V.

II. PINNED SPHERE-DIMER MOTORS

A. Continuum description

Chemically powered motors that are propelled by diffusiophoresis make use of asymmetric catalysis on the motor surface to drive propulsion.[29] A chemical reaction $A \rightarrow B$ on the catalytic portion of the motor produces inhomogeneous concentration fields of fuel A and product B in its vicinity, and this gives rise to a body force that generates fluid flows in the surrounding medium which lead to propulsion of the motor. In the continuum treatment of this mechanism, the concentration and fluid velocity fields are determined by the reaction-diffusion and Stokes equations, which can be solved analytically for spherical Janus motors with catalytic and noncatalytic hemispherical caps.

In the continuum theory, the velocity of the motor is given by $\boldsymbol{V} = -\langle \mathbf{v}^{(s)} \rangle_S$, in terms of the surface average of the slip velocity, $\mathbf{v}^{(s)}$. The slip velocity, which is the fluid velocity field at the outer edge of the boundary layer where the intermolecular interactions between the motor and the solute species vanish, is given by[29] $\mathbf{v}^{(s)} = -\frac{k_B T}{\eta} \Lambda \boldsymbol{\nabla}_s c_B$, where c_B is the concentration of species B, k_B is Boltzmann's constant, T is the temperature, η is the fluid viscosity, and the gradient is taken tangential to the surface. The factor Λ depends on the intermolecular potentials and is given by $\Lambda = \int_0^\infty dr\, r \times (e^{-\beta W_{BN}} - e^{-\beta W_{AN}})$. The continuum calculation for the sphere-dimer motor has been carried out, but the calculations are more involved due to the lack of spherical symmetry and require the use of a bispherical coordinate system.[30,31] The explicit forms of these solutions for the concentration and fluid flow fields[31] are not required here.

From a microscopic perspective, motor propulsion will emerge naturally when the solution is treated at a molecular level and interactions with the motor are fully accounted for by intermolecular forces. Provided that the molecular dynamics of the entire system satisfies the basic conservation laws of mass, momentum, and energy, the coupling between the forces on the motor and solvent reproduces the underlying molecular mechanism of diffusiophoresis. Such a microscopic description also naturally accounts for thermal fluctuations, a very important aspect of the dynamics for nanoscale motors.

The sphere-dimer motors considered in this study consist of catalytic C and noncatalytic N spheres linked by a rigid bond of length R.[32,33] The orientation of a rotor is given by the unit vector pointing from the N to C spheres, $\hat{\mathbf{u}}$. A chemical reaction $A + C \xrightarrow{k_M} B + C$ taking place on the catalytic sphere will produce inhomogeneous concentration fields $c_A(\mathbf{r})$ and $c_B(\mathbf{r})$ of the fuel A and product B species in the system. These species interact with the dimer spheres through intermolecular potentials, $W_{\alpha H}$, ($\alpha = A, B$ and $H = C, N$). For simplicity, here and below, we assume that the interaction potentials have a finite range r_S and satisfy $W_{AC} = W_{BC} = W_{AN} \neq W_{BN}$ so that the noncatalytic N sphere experiences concentration-dependent forces which propel the dimer, while the catalytic C sphere only serves to generate the concentration gradients in the system.

B. Collective dynamics of pinned dimers

If the center of mass of the dimer motor is fixed by a force or constraint, its velocity will be zero and it will pump fluid because the diffusiophoretic force still acts on the motor. Since only the center of mass is fixed, the dimer is free to rotate. However, since the concentration and fluid velocity fields are mirror-symmetric about planes through the sphere-dimer bond axis, the self-diffusiophoretic mechanism will not cause rotation of an isolated pinned dimer. If the time evolution of the dimer is governed by microscopic dynamics, or stochastic dynamics that accounts for thermal fluctuations, it will simply execute rotational Brownian motion: it is a sphere-dimer rotor.

The situation changes markedly if the system contains more than a single rotor. The concentration and hydrodynamic flow fields due to other rotors in the system will interact with the self-generated fields around a given rotor and break the axial symmetry. Torques due to the diffusiophoretic coupling will be generated, and active rotational motion will take place leading to interactions among the rotors. The nature of these collective effects due to such coupling among pinned sphere-dimers is studied in this paper using both coarse-grain microscopic and Langevin methods.

III. MICROSCOPIC SIMULATIONS OF COLLECTIVE DYNAMICS

A. Simulation method

The sphere-dimer rotors and fluid molecules are contained in a simulation box with lengths $L_x = 256$, $L_y = 64$, and $L_z = 32$, with periodic boundary conditions in the x- and y-directions and impermeable walls with bounce-back boundary conditions for the fluid particles in the z-direction. The system evolves in time through a concatenation of streaming and collision steps. The streaming steps involve Newtonian evolution through intermolecular interactions in the system, while the collision steps occur at discrete time intervals and account for multiparticle collisions (MPCs) among the fluid molecules.[34]

Each rotor sphere has a radius of $\sigma_S = 2$ and a mass of $m_S = 4\pi\sigma_S^3 n/3$, where $n = 10$ is the average fluid particle density in the system. The rotor spheres interact with fluid particles of types A and B, with mass $m = 1$, through repulsive Lennard-Jones potentials given by $W_{H\alpha}(r) = 4\epsilon_{\alpha\beta}[(\sigma_S/r)^{12} - (\sigma_S/r)^6 + 1/4]$ for $r \leq r_S$, and zero otherwise. The H and α indices take the values $H = C, N$, and $\alpha = A, B$. The cutoff radii $r_S = 2^{\frac{1}{6}}\sigma_S$ define boundary layers around the spheres within which sphere-fluid interactions take place. The interaction energies are chosen such that the propulsion force due to self-diffusiophoresis only occurs on the N sphere. Consequently, the C sphere interaction energies are equal, $\epsilon_{CA} = \epsilon_{CB} = 1$, while for the N sphere, we consider two cases: $\epsilon_{NB} = 0.1 < \epsilon_{NA} = 1$ and $\epsilon_{NB} = 1 > \epsilon_{NA} = 0.1$, which lead to different dynamics. The Λ parameter for these two potential parameter choices has the value $\Lambda_{B<A} = -\Lambda_{B>A} = 0.3070$. The rotor spheres are constrained by a rigid bond of length $d = 5$, and their centers of mass are fixed to a distance of $d_W = \sigma_S + 1$ above one of the walls by holonomic constraints. The orientational motions of the rotors are strongly confined to a plane parallel to the wall through stiff harmonic potentials on each rotor sphere with force constant $k_z = 1000$ acting perpendicular to the wall. The positions of the rotors are fixed so that a fluid particle cannot simultaneously interact with more than a single sphere; thus, the only interactions among motors are through collective solvent-mediated effects.

The interactions among fluid particles are accounted for by multiparticle collisions instead of intermolecular potentials. In multiparticle collision dynamics, particles are sorted into collision cells ξ with linear dimension a_0. At discrete times τ, using rotation operators for each cell, effective collisions among the particles change their velocities to postcollision values so as to conserve mass, momentum, and energy.[34–36]

There are chemical reactions, $A + C \xrightarrow{k_M} B + C$, on the catalytic spheres of each dimer which drive propulsion, as well as nonequilibrium reactions in the fluid phase, $B \xrightarrow{k} A$, which maintain the system in a nonequilibrium steady state. The reactions on the rotor catalytic spheres are carried out as follows: whenever a particle of species A reaches a distance r_C^+ infinitesimally outside the boundary layer of the sphere, its identity is changed to B with probability p_+. Below, we always choose $p_+ = 1$. Reactions $B \rightarrow A$ in the fluid phase are carried out by reactive multiparticle collision dynamics.[37] In this method, at the discrete times τ for multiparticle collisions, reactions in each collision cell are carried out by a birth-death Markov process. In particular, the probability that the reaction $B \xrightarrow{k} A$ occurs first in the time interval τ in collision cell ξ, followed by any other event, is $p_R = 1 - e^{-a_R^\xi \tau}$, with $a_R^\xi = k N_B^\xi$, where N_B^ξ is the number of B particles in cell ξ. The fluid phase reaction rate constants varied in the range of $k = 10^{-4} - 10^{-2}$.

All the results are expressed in dimensionless units of energy ϵ, mass m, distance σ, and time $t = \sqrt{m\sigma^2/\epsilon}$. In the simulations reported below, the MPC cell size and collision times are $a_0 = 1$ and $\tau = 0.1$, respectively, using a rotation angle of $\pi/2$. The temperature of the system is given by $k_B T = 0.2$. For these system parameters, self-diffusion coefficients and viscosity of the fluid are given by $D_A = D_B = D = 0.0233$ and $\eta = 5.085$, respectively. The velocity Verlet algorithm with a time step of $\Delta t = 0.005$ was used for the Newtonian evolution in the streaming steps of the evolution.

B. Screening by bulk reaction

Below, we consider various configurations of pinned sphere-dimer rotors, whereby a number of factors will determine the nature of the collective dynamics. An obviously important factor is the distance between rotors since this will determine how strongly they interact through both hydrodynamic and chemical interactions. The fluid phase reactions will play a role in the coupling through chemical fields for a given rotor separation due to screening effects.[38] For simplicity, consider a single catalytic sphere with reaction $A + C \xrightarrow{k_M} B + C$ in a medium with the bulk reaction $B \xrightarrow{k} A$. The local steady state concentration of species B (or A) may be determined from the solution of the reaction-diffusion equation, $D\nabla^2 c_B(r) = -k c_B(r)$ subject to the boundary condition $k_D R_C \hat{\mathbf{n}} \cdot \boldsymbol{\nabla} c_B(r)|_{R_C^+} = k_M^0 (c(R_C^+) - c_0)$, where $R_C^+ = r_C + \delta$ is a distance infinitesimally outside the interaction boundary layer around the C sphere, k_M^0 is an intrinsic reaction rate constant, and $k_D = 4\pi D R_C$ is the Smoluchowski diffusion controlled rate constant. An estimate for the intrinsic rate constant may be obtained from hard sphere collision theory, $k_M^0 = p_+ R_C^2 \sqrt{8\pi k_B T/m}$. For our system parameters $k_M^0 = 8.97$ and $k_D = 0.59$ and since $k_M^0 \gg k_D$, the reaction is diffusion controlled. In the boundary condition, we used $c_A + c_B = c_0$. Far from the sphere, $\lim_{r\to\infty} c_B(r) = 0$. The B concentration field obtained from the solution of the reaction-diffusion equation is

$$c_B(r) = \frac{k_M^0 k_D}{k_D(1 + \kappa R_C) + k_M^0} \frac{e^{-\kappa(r - R_C)}}{4\pi D r} c_0, \tag{1}$$

where $\kappa = \sqrt{k/D}$ corresponding to a screening length of $\ell_c = \kappa^{-1}$. Thus, for a given separation between rotors, κ will control the magnitude of the coupling through chemical gradients and is an important variable to consider. For the range of rate constant k values specified above, the screening length varies in the range of $1.53 \leq \ell_c \leq 15.27$.

A system with many pinned sphere-dimer rotors arranged randomly on a surface is expected to exhibit complex dynamics. We first consider the simple configuration of a periodic line of rotors for the two intermolecular potential cases mentioned above, $\epsilon_{NB} < \epsilon_{NA}$ and $\epsilon_{NB} > \epsilon_{NA}$, and study how the rotor separation and screening length modify the collective orientational dynamics of the chain. We then extend the study by briefly describing the collective behavior of two-dimensional arrays of pinned rotors.

C. Linear array of rotors

Consider a linear arrangement of N_r rotors along the x-direction with periodic boundary conditions, whose centers of mass are separated from each other by equal distances ℓ_s. The separation distance $\ell_s = L_x/N_r$ may be varied by changing the number of rotors. Letting $\ell_s = d + 2r_S + \sigma_{\text{sep}}$, we may define σ_{sep} as the smallest separation between the cutoff radii r_S of spheres of neighboring dimers, which is a useful measure of the proximity of dimer spheres. The character of the statistically stationary state depends on the relative magnitudes of the potential parameters, as can be seen in Fig. 1 (Multimedia view), which shows the metastable configurations that form during the dynamics. For $\epsilon_{BN} < \epsilon_{AN}$, the rotors exist in predominantly head-to-tail configurations oriented along the x axis although there are defects where the

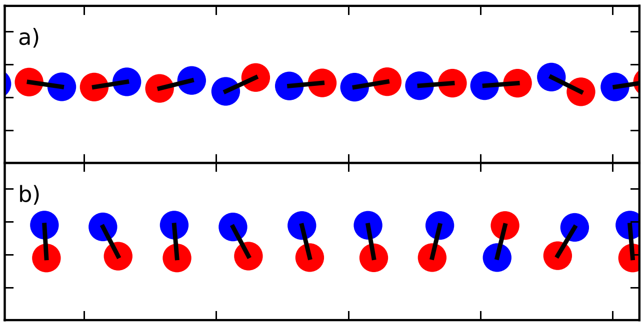

FIG. 1. The formation of metastable configurations of a segment of the periodic line of rotors separated by $\ell_s = 9.85$ with $\ell_c = 4.83$ for (a) $\epsilon_{AN} = 1$, $\epsilon_{BN} = 0.1$ and (b) $\epsilon_{BN} = 1, \epsilon_{AN} = 0.1$. Here and below, red will denote the catalytic sphere and blue will denote the noncatalytic sphere in a rotor. Multimedia view: https://doi.org/10.1063/1.5018297.1

direction of the head-to-tail ordering reverses. By contrast, when $\epsilon_{BN} > \epsilon_{AN}$, the rotors tend to align in stacks perpendicular to the x axis with their orientation vectors pointing in the same direction, again with defects where the orientations change directions, as well as other disordered spatial regions.

In qualitative terms, one can understand the propensity for motor systems with $\epsilon_{BN} < \epsilon_{AN}$ to order head-to-tail and motor systems with $\epsilon_{BN} > \epsilon_{AN}$ to order in stacks. When $\epsilon_{BN} < \epsilon_{AN}$, an isolated unpinned motor will move in the forward direction with the catalytic sphere at its head where the product concentration is higher. By contrast, when $\epsilon_{BN} > \epsilon_{AN}$, the motor will move in a backward direction with the noncatalytic sphere at its head where the product concentration is lower. In our dimer model, only the noncatalytic sphere experiences the diffusiophoretic forces due to concentration gradients. The head-to-tail arrangements are favored for forward-moving motors since deviations from this arrangement will tend to be removed by chemotactic forces that act on the N sphere which cause it to move towards higher product concentrations. Since the N spheres of backward-moving motors tend to move towards low product concentrations, the stacked configurations are consistent with the chemotactic forces in this case.

We now consider the quantitative aspects of the ordered configurations. The formation of ordered domains can be seen in the space-time plots in Fig. 2. Parts (a) for $\ell_s = 9.85$ and (b) for $\ell_s = 12.80$ show $\hat{u}_x(x,t) = \hat{\mathbf{x}} \cdot \hat{\mathbf{u}}(x,t)$, where $\hat{\mathbf{x}}$ is a unit vector along the positive x-direction, versus space and time for $\epsilon_{NB} < \epsilon_{NA}$. For the discrete rotor system, the space variable is defined by $x = j\ell_s$, with j the motor index taking the values $j = 1, \ldots, N_r$. The corresponding plots of $\hat{u}_y(x,t) = \hat{\mathbf{y}} \cdot \hat{\mathbf{u}}(x,t)$, where $\hat{\mathbf{y}}$ is a unit vector along the positive y-direction, are given in parts (c) and (d) of this figure for $\epsilon_{NB} > \epsilon_{NA}$. Starting from random initial orientations, provided that ℓ_s is not too large and screening length ℓ_c is not too small, one can observe the formation and persistence of ordered domains for times longer than the average reorientation time for an isolated rotor. It performs orientational Brownian motion with decorrelation time $\tau_R = 1/D_R = 4.67 \times 10^3$, where D_R is the rotational diffusion coefficient. The domains form very quickly from random orientations for both potential energy parameter choices when $\ell_s = 9.85$ ($\sigma_{\rm sep} = 0.36$) is small for this value of ℓ_c [parts (a) and (c) of the figure]. By contrast, if $\ell_s = 12.80$ ($\sigma_{\rm sep} = 3.31$) as in parts (b) and (d) of the figure, the propensity to form ordered domains is greatly reduced. The tendency to form the head-to-tail configurations is stronger than that for stacks of rotors since the N sphere is much closer to the C sphere of an adjacent rotor for head-to-tail configurations.

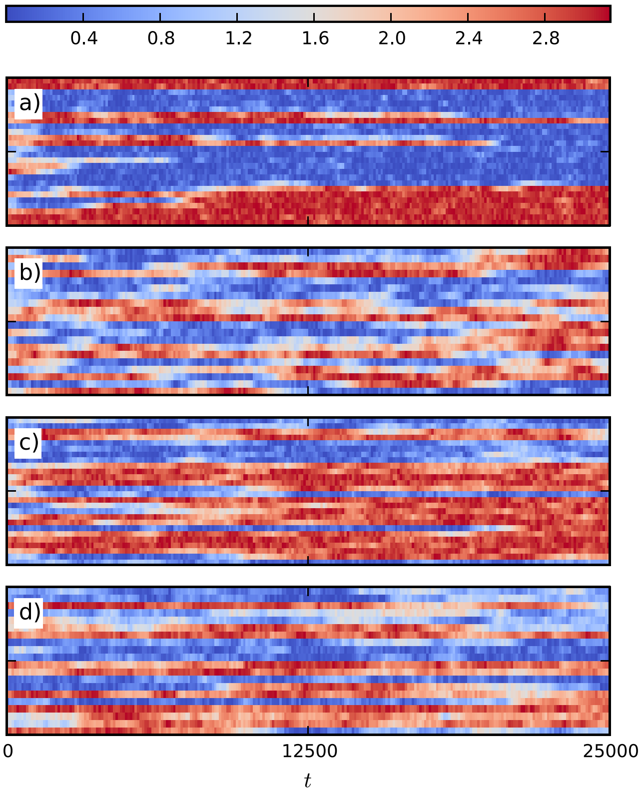

FIG. 2. Space-time plots of $\hat{u}_x(x,t)$ for a line of rotors from single trajectories with $\epsilon_{BN} < \epsilon_{AN}$ for (a) $\ell_s = 9.85$ and (b) $\ell_s = 12.80$ and plots of $\hat{u}_y(x,t)$ with $\epsilon_{BN} > \epsilon_{AN}$ for (c) $\ell_s = 9.85$ and (d) $\ell_s = 12.80$. The chemical screening length is $\ell_c = 4.83$ for all plots.

Additional information concerning the orientational correlations among different rotors can be obtained as follows: The angle θ^i_j between the orientation vector of rotor i, $\hat{\mathbf{u}}_i$, and the rotor $i+j$, $\hat{\mathbf{u}}_{i+j}$, is defined by $\cos\theta^i_j = \hat{\mathbf{u}}_i \cdot \hat{\mathbf{u}}_{i+j}$. We may then define the spatial correlation functions

$$S_m(j) = \frac{1}{N_r}\sum_{i=1}^{N_r}\langle P_m(\cos\theta^i_j)\rangle, \tag{2}$$

where P_m is the Legendre polynomial of order m and the angular brackets signify an average over time and realizations. Since the rotors tend to adopt orientations that are parallel or anti-parallel with respect to one another, $S_1(j)$ and $S_2(j)$ can be used to gauge the degree of alignment as a function of j for a given value of ℓ_s. For reference, the values $S_2 = 1, 0.25$ correspond to perfectly aligned (either parallel or antiparallel) and uncorrelated rotors, respectively. The quantity S_1, which takes the values $S_1(j) = -1, 1, 0$ for chains with antiparallel, parallel, and uncorrelated neighbours, respectively, can be used to give additional information about the alignment.

The values of $S_2(1)$ and $S_1(1)$ are given in Fig. 3 for different values of ℓ_s and ℓ_c. For both interaction potential

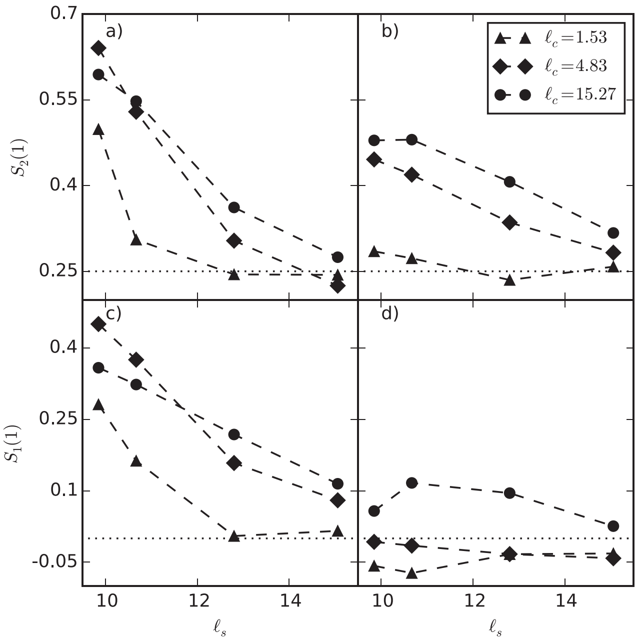

FIG. 3. Plots of $S_2(1)$ and $S_1(1)$ for different separations ℓ_s and chemical decay lengths ℓ_c for $\epsilon_{BN} < \epsilon_{AN}$ (head-to-tail) (a) and (c) and $\epsilon_{BN} > \epsilon_{AN}$ (stacks) (b) and (d). The dotted line corresponds to the uncorrelated rotors.

choices, the degree of alignment indicated by $S_2(1)$ is high when rotors are in close proximity, except for $\ell_c = 1.53$ for $\epsilon_{NB} > \epsilon_{NA}$. As expected, $S_2(1)$ decreases as ℓ_s increases and increases as ℓ_c increases, consistent with changes in the communication among the rotors as these lengths vary. The values of $S_1(1)$ are large for small ℓ_s for $\epsilon_{NB} < \epsilon_{NA}$, confirming the presence of large domains of head-to-tail configurations.

The variations of $S_2(j)$ with j for $\ell_s = 9.85$ and various values of ℓ_c are shown in Fig. 4 in (a) for $\epsilon_{NB} < \epsilon_{NA}$ and in (b) for $\epsilon_{NB} > \epsilon_{NA}$ and show that the strong correlations persist along the chain of rotors, again except for the smallest value of $\ell_c = 1.53$ for $\epsilon_{NB} > \epsilon_{NA}$.

1. Fluid velocity and concentration fields

In addition to the coupling arising from concentration gradients, pinned rotors pump fluid and induce velocity fields in their vicinity, which can lead to hydrodynamic coupling among the rotors. Visualization of these velocity and concentration fields as a function of time in the simulations is difficult because of the extensive averaging that must be carried out to account for the rotor configurational changes during the temporal evolution of the system. However, if the rotor positions are completely fixed in various configurations, these fields are easily extracted from the simulations.

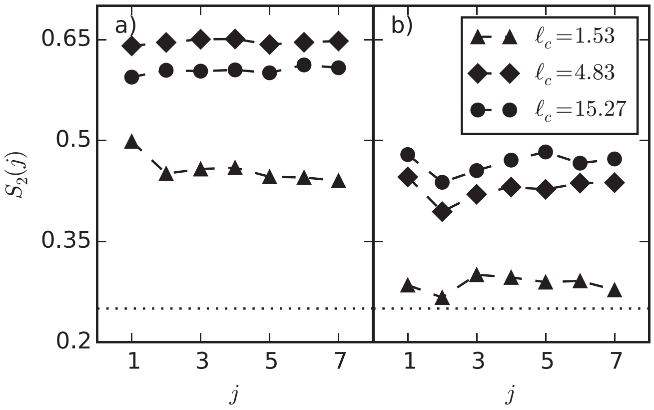

FIG. 4. Plots of $S_2(j)$ versus j for $\ell_s = 9.85$ and several values of ℓ_c for (a) $\epsilon_{BN} < \epsilon_{AN}$ (head-to-tail) and (b) $\epsilon_{BN} > \epsilon_{AN}$ (stacks). The dotted line corresponds to the uncorrelated rotors.

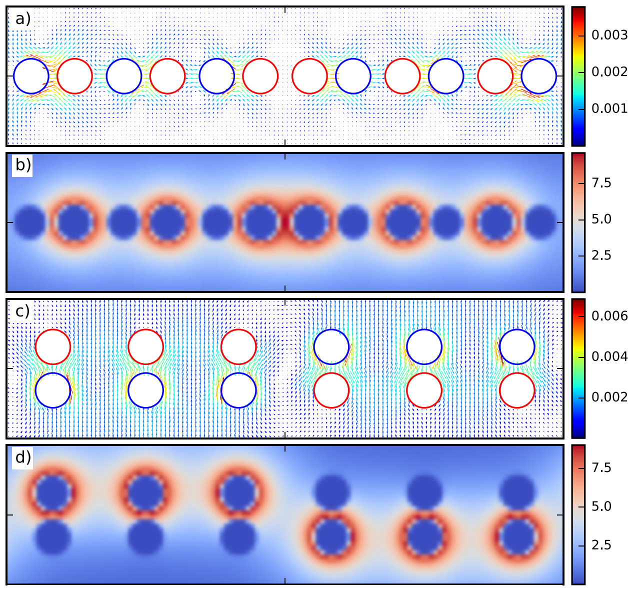

FIG. 5. Hydrodynamic flow (a) and (c) and concentration (b) and (d) fields in the xy-plane for a periodic line of six rotors with two defects for $\ell_c = 4.83$ and $\ell_s = 10.67$ with $\epsilon_{BN} < \epsilon_{AN}$ (a) and (b) and $\epsilon_{BN} > \epsilon_{AN}$ (c) and (d).

Figure 5 shows these fields in the xy-plane for $\ell_s = 10.67$ and $\ell_c = 4.83$ for both head-to-tail configurations with $\epsilon_{BN} < \epsilon_{AN}$ and stacked configurations with $\epsilon_{BN} > \epsilon_{AN}$. The corresponding fields for the xz-plane are shown in Fig. 6 for the head-to-tail configurations. The configurations have single defects to show how the velocity and concentration fields are altered in these regions. In both cases, the strongest fluid flow occurs around the N sphere in regions where the concentration gradients are greatest, consistent with the diffusiophoretic mechanism; this corresponds to a region in which the magnitude of the slip velocity reaches a maximum. In the case of the head-to-tail configurations, the fluid pumps inward toward the C sphere and outwards from the N sphere of each rotor, and due to the close proximity of adjacent rotors, the C-to-N direction of the flow also occurs for adjacent rotors in the same domain. Additionally, the fluid pumps toward the wall near the C sphere and away from the wall at the N sphere. At the rotor domain boundaries, the

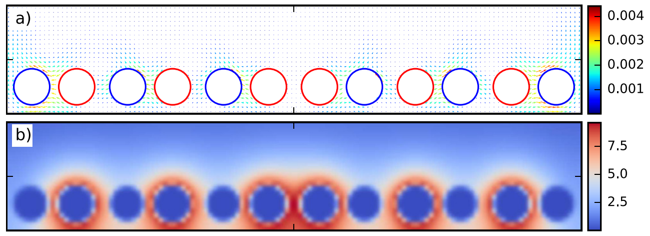

FIG. 6. Hydrodynamic flow (a) and concentration (b) fields in the xz-plane for a periodic line of six rotors with two defects for $\ell_c = 4.83$, $\ell_s = 10.67$, and $\epsilon_{BN} < \epsilon_{AN}$.

flow changes such that a reduced flow occurs at *C*–*C* defects and an increased flow occurs at *N*–*N* defects; fluid pumping is strongest for rotors at *N*–*N* domain boundaries. For the stack configuration, the fluid flows in the opposite direction from the *N* to *C* spheres of each rotor. Adjacent rotors in the same domain produce fluid flows that reinforce one another, leading to an increase in the overall magnitude of the fluid flow, while at defects, the velocity is greatly reduced since the flow fields oppose one another. In contrast to the rotors in head-to-tail configurations, the fluid flow is not strongest at the boundary but in regions within a domain. Overall, in both cases, the presence of defects introduces regions of increased or decreased fluid flow relative to a single, isolated stationary rotor.

2. Exclusion of chemical interactions

In order to gauge the magnitude of interactions among the rotors arising from concentration fields, this coupling can be removed by altering the dynamical model.[39] In the full dynamical model, the catalytic spheres on each rotor produce product *B* molecules which may then interact with the *N* spheres of rotors in the chain. These concentration fields are responsible for both self- and cooperative-diffusiophoretic effects. The model may be changed so that the *C* sphere of a rotor *i* catalyzes the reaction $A \rightarrow B_i$, where B_i is a product molecule specific to that rotor. It interacts with the *N* sphere of rotor *i* through an interaction potential with energy parameter ϵ_{BN} but interacts with the *N* spheres of other motors $j \neq i$ with interaction energy ϵ_{AN}. Thus, in this dynamical model, self-diffusiophoresis at each rotor is maintained, but a rotor $j \neq i$ will see the species B_i as another *A* particle, effectively eliminating coupling through chemical gradients along the chain. The fluid chemical reaction does not discriminate between the different B_i product species, and the $B_i \rightarrow A$ reactions are carried out as in the full model without regard to the index *i*.

The results of simulations of this model are compared with those of the full reactive dynamics in Fig. 7 where $S_2(j)$ is shown for $\ell_s = 9.85$ and $\ell_c = 4.83$ for the two potential energy selections (a) $\epsilon_{BN} < \epsilon_{AN}$ and (b) $\epsilon_{BN} > \epsilon_{AN}$. One can see that where chemical coupling is excluded, correlations are almost completely eliminated. Hydrodynamic interactions alone are insufficient to maintain the correlations for these parameter values.

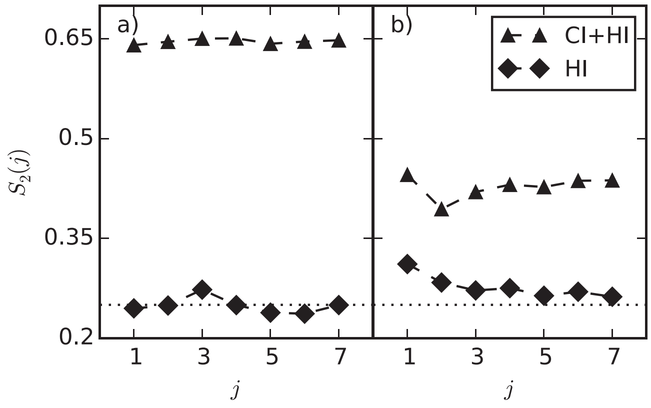

FIG. 7. Plot of $S_2(j)$ versus *j* with hydrodynamic interaction (HI) and with and without chemical interactions (CI) for $\ell_s = 9.85$ and $\ell_c = 4.83$ with (a) $\epsilon_{BN} < \epsilon_{AN}$ and (b) $\epsilon_{BN} > \epsilon_{AN}$. The dotted line corresponds to the uncorrelated rotors.

D. Two-dimensional array of rotors

The configurations adopted by the simple linear array of pinned rotors described above could be analyzed in some detail. Of course, the rotors may be pinned in two-dimensional random or regular arrays, and the variety of orientational configurations they may adopt as a result of chemical and hydrodynamic coupling is very large. A full exploration of the dynamics of these systems is beyond the scope of this study. However, in order to provide an indication of the orientational correlations that can arise in these systems, we show examples of some of the states that regular two-dimensional pinned rotors adopt.

Figure 8(a) shows that head-to-tail alignment occurs for $\epsilon_{BN} < \epsilon_{AN}$, similar to that in the one-dimensional system. For $\epsilon_{BN} > \epsilon_{AN}$ in panel (b), conformations form in which the *C* or *N* spheres of the rotors in 2×2 subarrays are oriented towards one another. In both cases, since the rotors have four nearest neighbours instead of two as in the periodic line, the structures that form are more dynamic and the rotors are able to switch between multiple metastable configurations.

IV. LANGEVIN MODEL

In order to provide additional insight into the interactions arising from chemical gradients in the system, we consider a Brownian dynamics model that approximately accounts for diffusiophoretic coupling among rotors while neglecting hydrodynamic interactions. The overdamped Langevin equation for the orientation of rotor *i* may be written as

$$\frac{d}{dt}\hat{\boldsymbol{u}}_i = \left[\boldsymbol{\zeta}_R^{-1} \cdot (\boldsymbol{T}_{di} + \boldsymbol{T}_{\mathrm{f}i})\right] \times \hat{\boldsymbol{u}}_i, \qquad (3)$$

where $\boldsymbol{T}_{di}$ is the torque acting on rotor *i* due to all other rotors in the system and $\boldsymbol{\zeta}_R$ is the rotational friction tensor. The random torque on this rotor arising from thermal fluctuations in the environment, $\boldsymbol{T}_{\mathrm{f}i}$, is a Gaussian, while noise processes with the zero mean and fluctuation dissipation relation

$$\langle \boldsymbol{T}_{Ri}(t)\boldsymbol{T}_{Rj}(t')\rangle = 2k_BT\boldsymbol{\zeta}_R\delta_{ij}\delta(t-t'). \qquad (4)$$

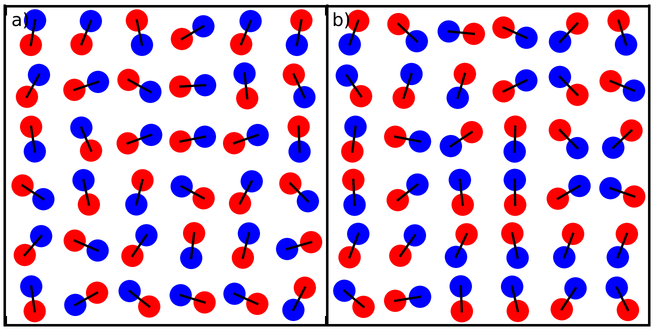

FIG. 8. Instantaneous configurations of the pinned rotors arranged in a periodic square lattice with the rotor separated by $\ell_s = 10.67$ with $\ell_c = 4.83$ for (a) $\epsilon_{BN} < \epsilon_{AN}$ and (b) $\epsilon_{BN} > \epsilon_{AN}$.

Since the rotors in our system are constrained by forces to rotate in the xy plane, the orientation vector takes the form $\hat{\boldsymbol{u}}_i = (\cos\phi_i, \sin\phi_i, 0)$, where ϕ_i is the polar angle of the rotor in this plane and $\hat{\boldsymbol{u}}_i \times \dot{\hat{\boldsymbol{u}}}_i = \hat{\boldsymbol{z}}\dot{\phi}_i$. In this case, Eq. (3) reduces to

$$\frac{d}{dt}\phi_i = \frac{1}{\zeta_R}(T_{di} + T_{Ri}), \tag{5}$$

where the z component of the torque is denoted by $T = \hat{\boldsymbol{z}} \cdot \boldsymbol{T}$ with $\hat{\boldsymbol{z}}$ a unit vector along z. The zz-component of the rotational friction tensor is simply denoted by ζ_R, and its value from simulation is $\zeta_R = 934$.

The torque T_{di} with contributions from all other rotors in the system must now be determined to construct the evolution equations. We make several assumptions to find this torque. The noncatalytic sphere of the i-th rotor will experience a diffusiophoretic force $\boldsymbol{F}_{di}$ from all other rotors, and we assume that this force is given by a superposition of $\boldsymbol{F}^j_{di}$, the forces on the noncatalytic sphere of rotor i due to rotors j

$$\boldsymbol{F}_{di} = \sum_{j \neq i} \boldsymbol{F}^j_{di}. \tag{6}$$

The resulting torque on rotor i is

$$T_{di} = \frac{d}{2}\sum_{j\neq i} \hat{\boldsymbol{z}} \cdot (\hat{\boldsymbol{u}}_i \times \boldsymbol{F}^j_{di}) = \frac{d}{2}\sum_{j\neq i} \sin\theta_{ij} F^j_{di}. \tag{7}$$

The second equality follows from the fact that the force $\boldsymbol{F}^j_{di}$ acts in the direction of the unit vector from the C sphere of rotor j to the N sphere of rotor i, $\hat{\boldsymbol{r}}^{NC}_{ij}$, where $\boldsymbol{r}^{NC}_{ij} = \boldsymbol{r}^N_i - \boldsymbol{r}^C_j$. We may then write $\boldsymbol{F}^j_{di} \equiv \hat{\boldsymbol{r}}^{NC}_{ij} F^j_{di}$ and use $\hat{\boldsymbol{u}}_i \times \hat{\boldsymbol{r}}^{NC}_{ij} = \sin\theta_{ij}\hat{\boldsymbol{z}}$, where θ_{ij} is the angle between $\hat{\boldsymbol{u}}_i$ and $\hat{\boldsymbol{r}}^{NC}_{ij}$, to obtain the second equality. The Langevin equation now reads

$$\frac{d}{dt}\phi_i = \frac{1}{\zeta_R}\left(\frac{d}{2}\sum_{j\neq i} \sin\theta_{ij} F^j_{di} + T_{Ri}\right). \tag{8}$$

To complete the evolution equation, we must specify the diffusiophoretic forces that enter Eq. (8). These quantities may be estimated as follows: The diffusiophoretic force on a sphere N in solution in a concentration gradient of B particles is given by $\boldsymbol{F}_d = \zeta_N \boldsymbol{V}_d$, with $\zeta_N = 6\pi\eta R_N$ being the friction coefficient of the sphere and $\boldsymbol{V}_d$ its diffusiophoretic velocity

$$\boldsymbol{V}_d = \frac{k_B T}{\eta}\overline{\Lambda(1 - \hat{\boldsymbol{n}}\hat{\boldsymbol{n}}) \cdot \boldsymbol{\nabla}_{\boldsymbol{r}} c_B(r)}^{\mathcal{S}}. \tag{9}$$

Here, $\hat{\boldsymbol{n}}$ is a unit normal to the sphere and the overline indicates an average over its surface $\mathcal{S}$.

In our rotor system, $\boldsymbol{F}^j_{di}$ depends on the concentration field generated by the C sphere of rotor j. Rewriting Eq. (9) to take this effect into account, we obtain

$$\boldsymbol{F}^j_{di} = \zeta_N \frac{k_B T}{\eta}\overline{\Lambda(1 - \hat{\boldsymbol{n}}_i\hat{\boldsymbol{n}}_i) \cdot \boldsymbol{\nabla}_{\boldsymbol{r}_i} c_B(|\boldsymbol{r}_i - \boldsymbol{r}^{NC}_{ij}|)}^{\mathcal{S}_i}. \tag{10}$$

Since c_B in Eq. (1) is defined with the C sphere as its origin, its argument in Eq. (10) accounts for this change of origin. The force component $F^j_{di} = \hat{\boldsymbol{r}}^{NC}_{ij} \cdot \boldsymbol{F}^j_{di}$ is

$$\begin{aligned} F^j_{di} &= -6\pi k_B T\Lambda\, \overline{\sin\theta_i \partial_{\theta_i} c_B(|R_N \hat{\boldsymbol{r}}_i - \boldsymbol{r}^{NC}_{ij}|)}^{\mathcal{S}_i}, \\ &= 6\pi k_B T\Lambda \int_{-1}^{1} d\mu_i\, \mu_i c_B(|R_N \hat{\boldsymbol{r}}_i - \boldsymbol{r}^{NC}_{ij}|), \end{aligned} \tag{11}$$

where $\mu_i = \cos\theta_i$.

Using Eq. (11) in Eq. (8), the orientational dynamics of the system of rotors may be computed. This model accounts for thermal orientational fluctuations and neglects hydrodynamic interactions. It accounts for the coupling among rotors through chemical concentration fields but assumes that these fields can be obtained by a superposition of contributions from each rotor, which are in turn computed approximately. It also neglects wall effects. Nevertheless, as we shall see, it is able to capture some of the main features of the collective dynamics. The parameters that enter this model are known analytically or may be computed from single rotor dynamics and are listed in Sec. III.

Space-time plots for the Langevin dynamics are presented in Fig. 9 for the same parameters used in Fig. 2 for the corresponding microscopic simulations. The results show the same qualitative features: domain formation is rapid for $\ell_s = 9.85$, especially for the head-to-tail configurations, and, as expected, the rotors are less highly correlated for the larger $\ell_s = 12.80$ separation. The effects of Langevin thermal noise on the metastable rotor conformations are also evident in the space-time plots and suggest that the head-to-tail configurations are more stable than the stacked configurations. Thus, the Langevin model without hydrodynamic

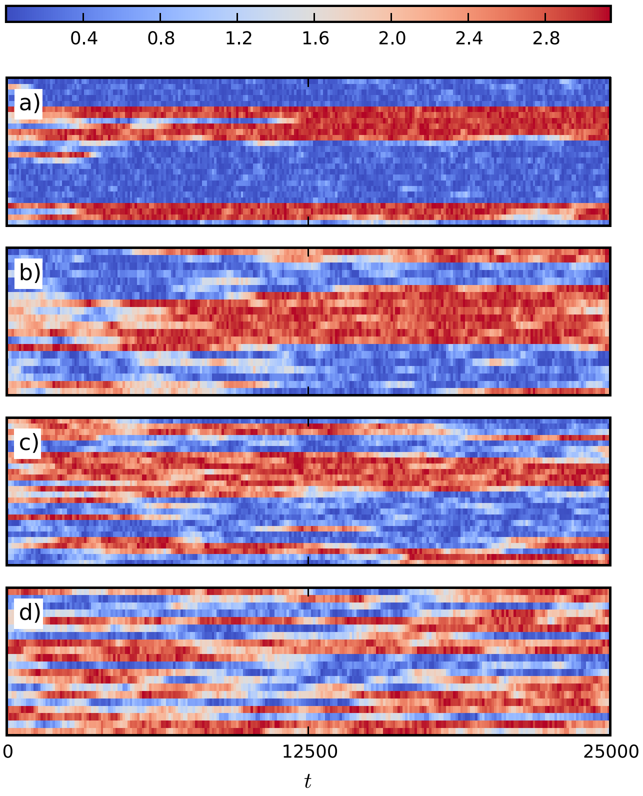

FIG. 9. Space-time plots for the Langevin dynamics of $\hat{u}_x(x,t)$ for a line of rotors from single trajectories with $\epsilon_{BN} < \epsilon_{AN}$ for (a) $\ell_s = 9.85$ and (b) $\ell_s = 12.80$ and plots of $\hat{u}_y(x,t)$ with $\epsilon_{BN} > \epsilon_{AN}$ for (c) $\ell_s = 9.85$ and (d) $\ell_s = 12.80$. The chemical screening length is $\ell_c = 4.83$ for all plots.

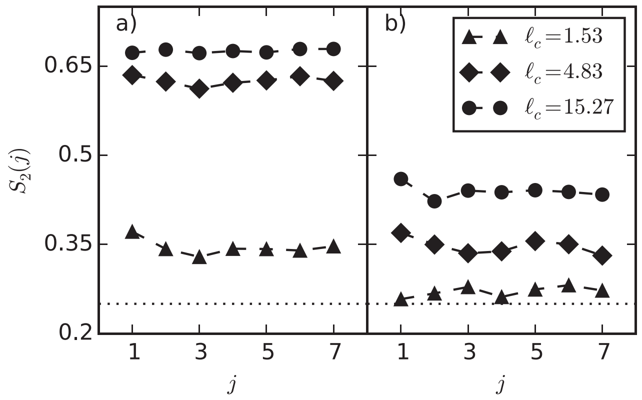

FIG. 10. Plots for the Langevin dynamics of $S_2(j)$ versus j for $\ell_s = 9.85$ and several values of ℓ_c for (a) $\epsilon_{BN} < \epsilon_{AN}$ and (b) $\epsilon_{BN} > \epsilon_{AN}$. The dotted line corresponds to the uncorrelated rotors.

interactions is able to capture qualitative features of the space-time plots seen in the microscopic simulations.

Similarities between the Langevin model and the microscopic simulation are also evident in the values of $S_m(j)$. Mirroring the same parameters as in Fig. 4, a plot of $S_2(j)$ as a function of j in Fig. 10 shows that correlations persist throughout the chain, with the head-to-tail configurations being far more correlated than the stack configuration for arbitrary ℓ_c. However, there are differences. In the microscopic simulation, the value of $S_2(j)$ for the head-to-tail configuration is higher for $\ell_c = 4.83$ than $\ell_c = 15.27$ but lower in the Langevin model. Nevertheless, the Langevin model is surprisingly excellent in capturing gross aspects of the collective behavior despite its simplicity.

V. CONCLUSIONS

Like the many-body dynamics of chemically powered motors in solution, such motors pinned to a surface also organize into distinct types of collective states, but the collective motions underlying these states are confined to orientational degrees of freedom. Both hydrodynamic flows arising from pinning of these active objects to the surface, and chemical concentration fields, whose gradients lead to active motion through the diffusiophoretic mechanism, can be responsible for coupling among the rotors. The discussion of the relative importance of these two effects is a common theme in attempts to understand the basis for the observed collective behavior in active matter comprising chemically self-propelled objects. The same issues arise in the consideration of the collective orientational dynamics of pinned self-propelled motors.

In this paper, we showed that these nonequilibrium active systems can self-organize into highly correlated orientational states whose structure is determined by the nature of the fluid interactions with the motor that determines whether the motor will move "forward" or "backward" when free in solution. The collective states also depend on the pinning configuration and the manner in which the nonequilibrium state is maintained. While both hydrodynamic flows and concentration fields are present, our results show that chemical fields play the most important role in determining the observed collective behavior. In other active rotor systems where the active rotors are not chemically propelled, only hydrodynamic effects operate and have been shown to lead to collective orientational behavior.[40]

The collective dynamics of pinned sphere-dimer motor systems can be studied experimentally. Sphere dimer motors with micro- and nanometer dimensions have been constructed in the laboratory, and the dynamics of a single motor in solution has been studied in some detail. The experiments also showed that the dimer motors made from silica and platinum components may become pinned to a glass substrate due to strong interactions of the silica sphere with the surface. These pinned dimers execute active rotational dynamics with frequencies of several Hertz.[33] In addition, one of the first reports of synthetic nanorod motors described their rotational dynamics when pinned to surfaces.[14] The rotational dynamics of pinned motors takes place in the same parameter domains as the translational motion; thus, it should be possible to construct arrays of such pinned motors and observe their dynamics. The range of orientational collective phenomena increases substantially when higher dimensional arrays of pinned motors are considered. The relative importance of hydrodynamics and chemistry in these more complicated active rotor systems merits further study.

ACKNOWLEDGMENTS

This research was supported in part by a grant from the Natural Sciences and Engineering Research Council of Canada and through the research training group GRK 1558 funded by Deutsche Forschungsgemeinschaft. Computations were supported by Compute Canada and performed at the SciNet HPC Consortium.

We would also like to dedicate this article to Jack Hudson, a friend and scholar. He was a pioneer in the field of nonlinear chemical instabilities and did much to foster science in this area, and his work will have a lasting impact on the field.

[1] R. A. L. Jones, *Soft Machines: Nanotechnology and Life* (Oxford University Press, Oxford, 2004).
[2] E. M. Purcell, "Life at low Reynolds number," Am. J. Phys. **45**, 3 (1977).
[3] B. Alberts, D. Bray, J. Lewis, M. Raff, K. Roberts, and J. D. Watson, *Molecular Biology of the Cell*, 3rd ed. (Garland Science, 2002).
[4] J. Wang, *Nanomachines: Fundamentals and Applications* (Wiley-VCH, Weinheim, 2013).
[5] W. Wang, W. Duan, S. Ahmed, T. E. Mallouk, and A. Sen, "Small power: Autonomous nano- and micromotors propelled by self-generated gradients," Nano Today **8**, 531–554 (2013).
[6] R. Kapral, "Perspective: Nanomotors without moving parts that propel themselves in solution," J. Chem. Phys. **138**, 020901 (2013).
[7] S. Sánchez, L. Soler, and J. Katuri, "Chemically powered micro- and nanomotors," Angew. Chem., Int. Ed. **54**, 1414–1444 (2014).
[8] E. Lauga and T. R. Powers, "The hydrodynamics of swimming microorganisms," Rep. Prog. Phys. **72**, 096601 (2009).
[9] M. C. Marchetti, J. F. Joanny, S. Ramaswamy, T. T. Liverpool, J. Prost, M. Rao, and R. A. Simha, "Hydrodynamics of soft active matter," Rev. Mod. Phys. **85**, 1143 (2013).
[10] J. Elgeti, R. G. Winkler, and G. Gompper, "Physics of microswimmers - single particle motion and collective behavior: A review," Rep. Prog. Phys. **78**, 056601 (2015).
[11] A. Zöttl and H. Stark, "Emergent behavior in active colloids," J. Phys.: Condens. Matter **28**, 253001 (2016).

[12] C. Bechinger, R. D. Leonardo, H. Löwen, C. Reichhardt, G. Volpe, and G. Volpe, "Active particles in complex and crowded environments," Rev. Mod. Phys. **88**, 045006 (2016).

[13] W. F. Paxton, K. C. Kistler, C. C. Olmeda, A. Sen, S. K. S. Angelo, Y. Cao, T. E. Mallouk, P. E. Lammert, and V. H. Crespi, "Catalytic nanomotors: Autonomous movement of striped nanorods," J. Am. Chem. Soc. **126**, 13424–13431 (2004).

[14] S. Fournier-Bidoz, A. C. Arsenault, I. Manners, and G. A. Ozin, "Synthetic self-propelled nanorotors," Chem. Commun. **4**, 441–443 (2005).

[15] M. Ibele, T. Mallouk, and A. Sen, "Schooling behavior of light-powered autonomous micromotors in water," Angew. Chem., Int. Ed. **48**, 3308–3312 (2009).

[16] I. Theurkauff, C. Cottin-Bizonne, J. Palacci, C. Ybert, and L. Bocquet, "Dynamic clustering in active colloidal suspensions with chemical signaling," Phys. Rev. Lett. **108**, 268303 (2012).

[17] J. Palacci, S. Sacanna, A. P. Steinberg, D. J. Pine, and P. M. Chaikin, "Living crystals of light-activated colloidal surfers," Science **339**, 936 (2013).

[18] I. Buttinoni, J. Bialké, H. Löwen, C. Bechinger, and T. Speck, "Dynamical clustering and phase separation in suspensions of self-propelled colloidal particles," Phys. Rev. Lett. **110**, 238301 (2013).

[19] W. Wang, W. Duan, A. Sen, and T. E. Mallouk, "Catalytically powered dynamic assembly of rod-shaped nanomotors and passive tracer particles," Proc. Natl. Acad. Sci. U.S.A. **110**, 17744 (2013).

[20] O. Pohl and H. Stark, "Dynamic clustering and chemotactic collapse of self-phoretic active particles," Phys. Rev. Lett. **112**, 238303 (2014).

[21] O. Pohl and H. Stark, "Self-phoretic active particles interacting by diffusiophoresis: A numerical study of the collapsed state and dynamic clustering," Eur. Phys. J. E **38**, 93 (2015).

[22] S. Saha, R. Golestanian, and S. Ramaswamy, "Clusters, asters, and collective oscillations in chemotactic colloids," Phys. Rev. E **89**, 062316 (2014).

[23] B. Liebchen, M. E. Cates, and D. Marenduzzo, "Pattern formation in chemically interacting active rotors with self-propulsion," Soft Matter **12**, 7259–7264 (2016).

[24] B. Liebchen, D. Marenduzzo, and M. E. Cates, "Phoretic interactions generically induce dynamic clusters and wave patterns in active colloids," Phys. Rev. Lett. **118**, 268001 (2017).

[25] S. Thakur and R. Kapral, "Collective dynamics of self-propelled sphere-dimer motors," Phys. Rev. E **85**, 026121 (2012).

[26] P. Colberg and R. Kapral, "Many-body dynamics of chemically-propelled nanomotors," J. Chem. Phys. **147**, 064910 (2017).

[27] M.-J. Huang, J. Schofield, and R. Kapral, "Chemotactic and hydrodynamic effects on collective dynamics of self-diffusiophoretic janus motors," New J. Phys. **19**, 125003 (2017).

[28] A. Scagliarini and I. Pagonabarraga, "Non-equilibrium phases in suspensions of self-propelled colloidal particles controlled by phoretic mobility and hydrodynamics," e-print arXiv:1605:03773.

[29] J. L. Anderson, "Colloid transport by interfacial forces," Phys. Fluids **26**, 2871 (1983).

[30] M. N. Popescu, M. Tasinkevych, and S. Dietrich, "Pulling and pushing a cargo with a catalytically active carrier," Europhys. Lett. **95**, 28004 (2011).

[31] S. Y. Reigh and R. Kapral, "Catalytic dimer nanomotors: Continuum theory and microscopic dynamics," Soft Matter **11**, 3149–3158 (2015).

[32] G. Rückner and R. Kapral, "Chemically powered nanodimers," Phys. Rev. Lett. **98**, 150603 (2007).

[33] L. F. Valadares, Y.-G. Tao, N. S. Zacharia, V. Kitaev, F. Galembeck, R. Kapral, and G. A. Ozin, "Catalytic nanomotors: Self-propelled sphere dimers," Small **6**, 565–572 (2010).

[34] A. Malevanets and R. Kapral, "Mesoscopic model for solvent dynamics," J. Chem. Phys. **110**, 8605–8613 (1999); A. Malevanets and R. Kapral "Solute molecular dynamics in a mesoscale solvent," *ibid.* **112**, 7260–7269 (2000).

[35] R. Kapral, "Multiparticle collision dynamics: Simulation of complex systems on mesoscales," Adv. Chem. Phys. **140**, 89–146 (2008).

[36] G. Gompper, T. Ihle, D. M. Kroll, and R. G. Winkler, *Multi-Particle Collision Dynamics: A Particle-Based Mesoscale Simulation Approach to the Hydrodynamics of Complex Fluids*, edited by C. Holm and K. Kremer (Advanced Computer Simulation Approaches for Soft Matter Sciences III, Advances in Polymer Science, Springer, Berlin, Heidelberg, 2009), Vol. 221.

[37] K. Rohlf, S. Fraser, and R. Kapral, "Reactive multiparticle collision dynamics," Comput. Phys. Commun. **179**, 132–139 (2008), special issue based on the Conference on Computational Physics 2007.

[38] S. Thakur and R. Kapral, J. Chem. Phys. **135**, 024509 (2011).

[39] M.-J. Huang and R. Kapral, "Collective dynamics of diffusiophoretic motors on a filament," Eur. Phys. J. E **39**, 36 (2016).

[40] N. Uchida and R. Golestaniani, "Synchronization and collective dynamics in a carpet of microfluidic rotors," Phys. Rev. Lett. **104**, 178103 (2010).